Surface Diffusion Barriers and Catalytic Activity Driven by Terminal Groups at Zeolite Catalysts

Mingbin Gao, Hua Li, Yu Tian, Junyi Yu, Mao Ye,* and Zhongmin Liu
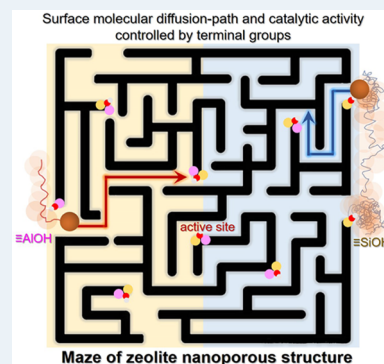
Read Online

ACCESS | Metrics & More | Article Recommendations | Supporting Information

ABSTRACT: Defects that commonly exist on the surface of zeolites pose notable mass transport constraints and influence the catalytic performance. The mechanism underlying the surface defects inducing molecular transport limitations, however, is not fully understood. Herein, we use versatile spectroscopy, imaging techniques, and multiscale simulations to investigate the effect of surface defects on the molecular surface transport in zeolites, intending to establish the terminal structure—mass transport—performance relationship. Isolated silanol, which represents the foremost and eventual chemical defective accessible site at zeolite termination for guest molecules from the bulk fluid phase into zeolites or vice versa, is taken as a showcase. We demonstrate that isolated silanol at H-SAPO-34 zeolite termination not only enhances the adsorptive interaction between the polar molecules/alkenes and interface but also narrows the local 8-membered-ring pore at the external surface. The exterior surface with more isolated silanol could cause a higher diffusion barrier and hamper the accessibility of intracrystalline active sites. This work is expected to shed light on the mechanism underlying the zeolite catalyst upgrading via terminal surface modifications at zeolites.

Surface molecular diffusion-path and catalytic activity controlled by terminal groups

Maze of zeolite nanoporous structure

1. INTRODUCTION

Zeolites are most critical solid catalysts, which are widely used in petrochemical upgrading,[1−5] energy transition,[6] and CO_2 capture.[7,8] In the long-term exploitations of zeolites, defects have been regarded as the foremost feature in affecting the performance of zeolite catalysts.[9,10] Chemical defects, e.g., hydroxyls, result from the presence of heteroatoms on a neutral framework necessarily balanced by an extra framework charge or the break of periodic units of TO_4 (T = Si, Al,···).[9,11] Such defects are the origin of the remarkable properties of zeolites in acid catalysis.[12] Structural defects at the zeolite boundary, e.g., amorphous phase,[13−15] mismatching in pore alignment,[13,16] and blocking surface pore entrances,[17,18] are proposed as one of the vital dimensions to modulate the mass transport in zeolites.[16,19,20] Therefore, deciphering defects at surface termination is highly concerned in zeolite catalysts so far.[13,14,18,21−23] An urgent demand is found in exploring the relationship between the crystalline-terminated structure and performance for precisely tailoring the properties of zeolites.[9,10,15]

Currently, considerable endeavors have been undertaken to visualize non-ideal structure defects at zeolite termination and found that such structure defects would cause molecular diffusion barriers (or surface barriers).[13,16] For instance, Karwacki et al.[13] implemented confocal fluorescence microscopy (CFM), transmission electron microscopy (TEM), and atomic force microscopy (AFM); it was found that amorphous and pore alignment at the external surface of zeolites can cause

the presence of molecular diffusion barriers. Han et al.[16,24] directly observed the breaking of the periodic structure at the boundary of metal−organic frameworks at the atomic level by use of high-resolution TEM (HR-TEM), and they found that such structure defects would impede molecular diffusion. Apparently, introducing well-defined defects at zeolite termination can be used to modulate surface barriers. However, constructing such non-ideal layers at zeolite termination is a nontrivial task. It has been demonstrated that the existence of breaks in the connection between TO_4 units or periodic association in such a layer inevitably results in abundant chemical defects at the terminal surface.[9−11] Isolated silanol ($\equiv$Si−O−H), which frequently functions as a terminal group to complete the valence of oxygen atoms of TO_4 units, represents the foremost or eventual accessible sites for reactants/products from a fluid phase into zeolites or vice versa. Unfortunately, the effect of isolated silanol as archetypal terminal groups on surface barriers in zeolites has been rarely noticed, especially. How isolated silanol affects the local structure/properties and surface diffusion path of guest molecules at the zeolite exterior surface needs to be unveiled.
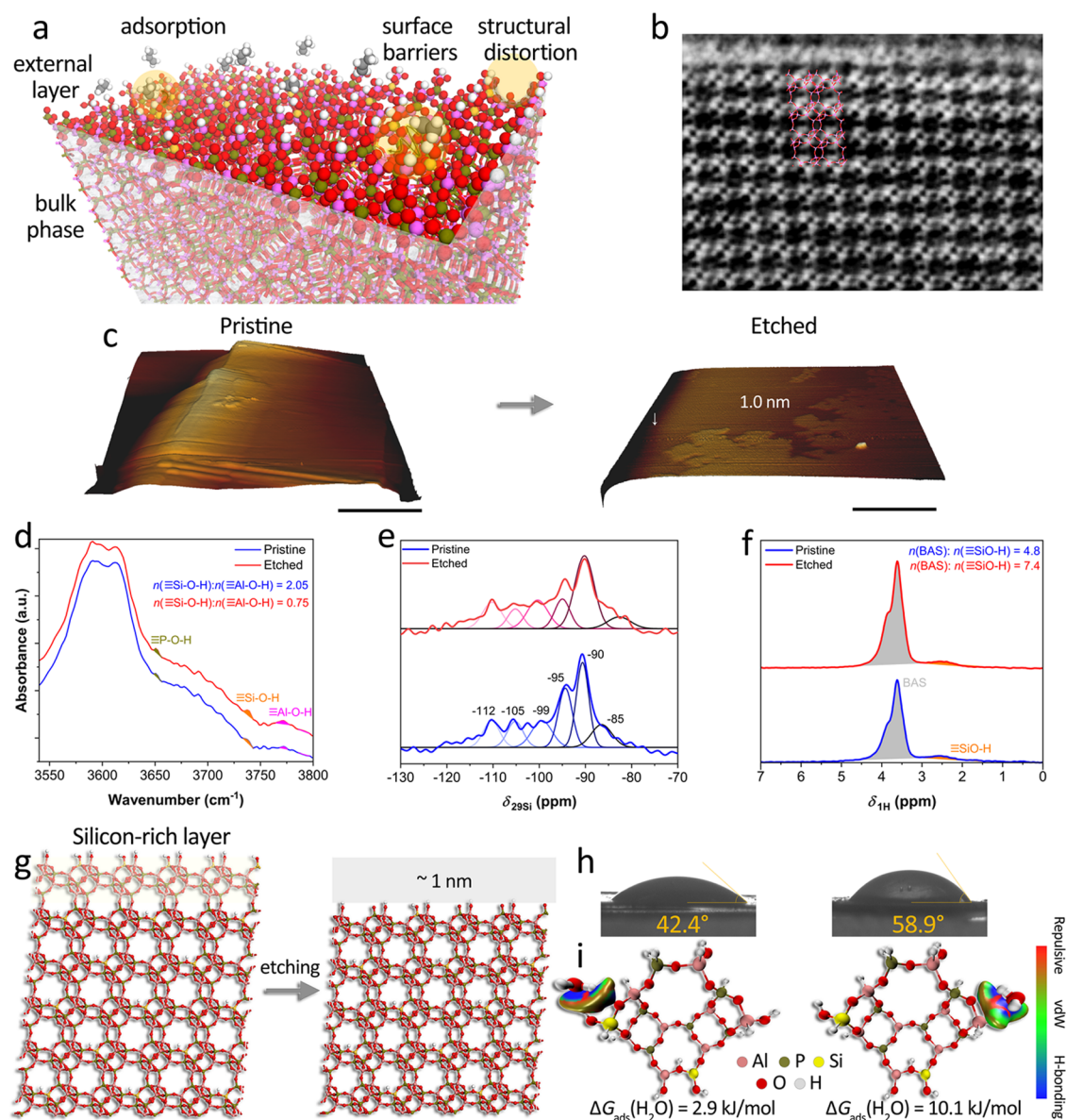
Figure 1. (a) Scheme of the effect of isolated silanol on the local structure, molecular adsorption, and diffusion at zeolite termination. (b) iDPC-STEM image of external and internal regions of H-SAPO-34 zeolites. (c) Microtopography of pristine and etched H-SAPO-34 zeolite imaged by AFM. (d) Hydroxyl functional groups of pristine and etched H-SAPO-34 zeolite detected by DRIFT. (e, f) ^{1}H and ^{29}Si MAS NMR spectra of pristine and etched H-SAPO-34 samples, respectively. (g) Proposed models of the crystal boundary of pristine (rich in isolated silanol) and etched H-SAPO-34 zeolite. (h) Contact angle of water droplets at pristine (left) and etched (right) H-SAPO-34 zeolite. (i) Isosurface plots of the reduced density gradient[37] and adsorption energy for the water adsorbed at $\equiv$Si−O−H (left) and $\equiv$Al−O−H (right) groups based on the DFT calculations over 16T cluster model.

Meanwhile, emerging studies show that surface barriers can dominate mass transfer resistance[18,25,26] and significantly influence zeolite catalysis. Synthetic, e.g., epitaxial growth of fin-like protrusions on the external surface[22,27] and siliceous layer at the exterior rim,[15] and postsynthetic surface modifications, e.g., chemical liquid/vapor deposition,[20,28,29] moderate etching,[28,30] and grafting of chemical groups,[31] can be employed to modulate the surface permeability of guest molecules. Importantly, improving molecular surface permeability can markedly enhance catalytic activity (conversion of *n*-alkane isomerization,[29] conversion of olefin cracking,[32] and reaction rate of propane in dehydrogenation[27]) and durability (lifetime of methanol to olefins[28] and carbonylation of dimethyl ether[30]). Conversely, reducing the surface perme-

ability of intermediate species trapped within zeolite can contribute greatly to the conversion of the inert reactant, e.g., conversion of methane with hydrogen peroxide to methanol.[31] In fact, how the regulated surface structure/properties induce different surface permeabilities of guests and the molecular mechanism of surface barriers on catalysis both remain ambiguous. In turn, the lack of explicit defect−mass transfer−performance relationship constrains the precise surface modifications for zeolite catalysts.[33,34]

In this work, we focus on how surface diffusion barriers are induced by the presence of isolated silanol. Furthermore, the detailed reaction diffusion courses controlled by different surface barrier behaviors related to a distinct amount of isolated silanol are unveiled. Industrially important H-SAPO-

34 zeolite was used as a host material, and the moderate etching method was used to modulate isolated silanol at the external surface. Multiple spectroscopic and microscopy techniques are implemented to examine the atomic structure, microtopography, composition, coordination, and functional groups of surface termination. External surface models deciphered by well-designed characterizations are used as input for multiscale modeling approaches, including ab initio molecular static and dynamic simulations (AIMD), force-field molecular dynamics (FFMD) and reaction diffusion model of the single zeolite crystal. Results show that isolated silanol not only strengthens the interaction between guests and the interface but also narrows the local 8-membered-ring (MR) pore, which reduces the surface permeability of both olefins and alkanes. Significant acceleration in coke deactivation and low accessibility of intracrystalline acid sites within the individual H-SAPO-34 crystal by olefin polymerization is observed due to the depressed surface permeability. Diffusion measurements and super-resolution structural illumination imaging (SIM) were used to validate and supplement the details of multiscale simulations. Conclusions indicate that modifying chemical groups[31] at zeolite termination could have notable influence on the molecular surface permeation and catalytic activity. The above-mentioned combination provides a complete picture of the terminal group−surface barrier−catalytic activity relationship (Figure 1a). Such a hybrid method could become an indispensable tool for the illumination of microscopic structure−molecular transport−material performance and facilitate, to a great extent, the upgrade of zeolite catalysts from the perspective of molecular traffic.

2. EXPERIMENTAL SECTION

2.1. Zeolite Materials and Characterizations. The synthesis procedure of H-SAPO-34 zeolites used in the experiments was reported in our previous studies.[35] Pseudo-boehmite (67.0 wt %) was first dissolved into distilled water, followed by the addition of an organic template of phosphoric acid (85.0 wt %), silica sol (31.0 wt %), and morpholine. The molar compositions of reagents were $2.0MOR:0.4-SiO_2:1.0Al_2O_3:1.0P_2O_5:30.0H_2O$. The final reactant gel was transferred to a Teflon-lined stainless-steel autoclave and heated at 200 °C for 48 h under rotation. The moderate etching at the zeolite surface was carried out as follows: 0.5 g of pristine H-SAPO-34 zeolites was added to 10.0 mL of acetic acid solution (0.02 mol/L). After magnetic stirring of the mixture at 333 K for 3 h, the slurry was filtered and dried at 393 K in air for 12 h. The sample was calcined at 823 K for 6 h to remove the organic template. The bulk phase purity, composition, and textural properties of zeolite samples were examined by X-ray diffraction (XRD), X-ray fluorescence (XRF), and nitrogen adsorption−desorption experiments, respectively. The atomic structure at the terminal surface of H-SAPO-34 was observed by integrated differential phase contrast (iDPC) scanning transmission electron microscopy (STEM). The chemical coordination information of H, Al, Si, and P and the amount of acidity in zeolite samples were measured by solid-state nuclear magnetic resonance (ssNMR). The microtopography and composition and composition gradient at the zeolite external surface were detected by atomic force microscopy (AFM), X-ray photoelectron spectroscopy (XPS), and energy-dispersive X-ray spectroscopy (EDS). The fingerprint peaks around 3500−3800 cm^{-1} of

chemical groups were measured by diffuse reflectance infrared Fourier transform (DRIFT). The uptake/desorption rate and isothermal adsorption curves of propylene and propane in zeolite samples were measured using an intelligent gravimetric analyzer (IGA). The measured products of IGA are well introduced in the reference.[36] The details of these characterizations are presented in Sections 1 and 2 of the Supporting Information.

2.2. Propylene Polymerization Catalyzed by Zeolites. The time evolutions of the intermediate and BAS within zeolite samples during the propylene polymerization reaction at 373 K were measured by DRIFT (Bruker Vextex70 spectrometer equipped with a MCT detector). The details of the experiment procedure are presented in Section 3 of the Supporting Information. The spatial temporal evolutions of coke species within zeolite samples during the propylene polymerization reaction were measured by super-resolution fluorescence imaging SIM. The super-resolution imaging was carried out using a Nikon N-SIM super-resolution microscopy system with a motorized inverted microscopy ECLIPSE Ti2-E, a ×100/NA 1.49 oil immersion TIRF objective lens (CFI HP) and ORCA-Flash 4.0 sCMOS camera (Hamamatsu Photonics K.K.). The wavelengths of illumination and emission detection of SIM used in this work are 405 (detection at 435−485 nm), 488 (detection at 500−545 nm), 561 (detection at 570−640 nm), and 640 nm (detection at 663−738 nm). Images were taken at a Z-plane of middle of the zeolitic crystal (∼1 μm). NIS-Elements Ar and N-SIM Analysis were used to analyze the collected images. The coke contents of deactivated SAPO-34 samples were measured by thermogravimetric analysis (TGA, SDTQ 600) at a temperature range of 323−1173 K with a heating rate of 15 K min^{-1} under an air flow of 100 mL min^{-1}. Here, the coke content is defined as the quantity of carbonaceous species per unit mass of the calcined catalyst, and thus, the loss of mass between 573 and 1173 K measured by TGA was used to estimate the coke content.

3. THEORETICAL CALCULATION

3.1. Density Functional Theory (DFT) Calculations. The adsorption energy of propylene, propane, and water at ≡Si−O−H and ≡Al−O−H groups was calculated by DFT. 16T cluster $(Al_8P_6Si_2O_2H_{22})$ models represent that the local structure of CHA zeolite is used to calculate the adsorption energies. The isosurface plots of the reduced density gradient (RDG) were obtained by calculating the RDG functions through Multiwfn software.[37] The transition state and free energy barrier of polymerization of propylene and cyclization of the coke precursor within H-SAPO-34 zeolite were calculated by DFT. For the calculation of the transition state, an extended 74 T $(SiP_{36}Al_{37}O_{119}H_{59})$ cluster model extracted from the crystallographic CHA structure represents the structure of neutral H-SAPO-34 model containing one Brønsted acid site. All DFT calculations were performed with the Gaussian 09 package.[38] The details of the DFT calculations are presented in Section 4 of the Supporting Information.

3.2. Molecular Dynamics (MD) Simulations. Ab initio molecular dynamics (AIMD) simulations were implemented to obtain free energy barrier profiles of propylene from the gas phase, external adsorption layer, external pore structure, and intracrystalline region with the consideration of the effect of BAS, ≡Si−O−H, and ≡Al−O−H groups. To measure the free energy profiles of propylene from the external surface to

the intracrystalline structure of H-SAPO-34 molecular sieves, AIMD simulations were performed using the CP2K software package (version 7.1).[39,40] The details of the AIMD simulations are presented in Section 5 of the Supporting Information. FFMD simulations were used to simulate the microarea uptake process of propylene from the gas phase to intracrystalline with the consideration of the effect of $\equiv$Si−O−H[41] and $\equiv$Al−O−H groups. The force field molecular dynamics (FFMD) approach was used to simulate the diffusion process of propylene in contact with a model H-SAPO-34 framework with explicit terminal groups at the surface using the Materials Studio simulation package (Accelrys Software). The details of the FFMD simulations are presented in Section 6 of the Supporting Information. Table S1 shows the XRF results, which indicates that the (P + Al)/Si is 9 for both bulk fresh and etched samples. It can be further estimated that there are 6 Al and 6 P atoms in a basic cell. Thus, it can be anticipated that a basic cell unit used for simulations contains 1 Si atom, which is close to the experimental results of XRF.

3.3. Reaction Kinetics−Mass Transfer Simulations.
The reaction kinetics of propylene polymerization within H-SAPO-34 zeolite were obtained by the transition-state calculations of DFT.[42,43] The surface permeability and intracrystalline diffusivity of propylene were obtained by IGA experimental measurement. The spatiotemporal evolutions of propylene and coke species within the H-SAPO-34 zeolite crystal were simulated by the in-house developed code.[35] The details of the equations and simulations are presented in Section 7 of the Supporting Information.

4. RESULTS AND DISCUSSION

4.1. Structure and Chemistry at the Zeolite Terminal Interface.
Modification of the external zeolite surface by moderate acid etching is an efficient method to alter surface barriers.[28] First, H-SAPO-34 zeolites were hydrothermally synthesized and named as "pristine" sample. Then, parts of the pristine sample were etched with acetic acidic solution and denoted as "etched" sample. The bulk information of these two samples is summarized in Table S1, and the bulk properties of pristine and etched H-SAPO-34 samples are almost consistent. In Figure 1b, the iDPC-STEM image shows the discrepant atomic structure of termination from that of the intracrystalline region, which represents the breaking of TO_4 units at the external surface. As shown in Figure 1c, by use of AFM, it can be directly observed that the thickness at the external surface of etched H-SAPO-34 is thinner, ~1.0 nm, than that of pristine H-SAPO-34. This implies that the acid etching method can exclusively remove the external substance from the pristine sample. XPS can detect the elemental composition (Si, Al, and P in this work) from a ~0.7 nm-deep external surface region of zeolites.[13] As shown in Figure S4, the integral area of XPS Si 2p spectra for pristine H-SAPO-34 is significantly higher than that for the etched H-SAPO-34. The graded distribution of Si, Al, and P elements from the external surface to the internal of these two samples was examined by EDS. In Figure S5, for the pristine sample, a steep gradient of Si close to the external surface can be observed and decreases from the external surface to the internal. In fact, Tian et al.[44] also found a nonuniform distribution of Si atoms in the crystals, which demonstrates a gradual increase from the core to the external surface, during secondary nucleation in the crystallization of SAPO-34 zeolites. However, the distribution of Si within the etched H-SAPO-34 crystal is relatively uniform. Based on the

above-mentioned evidence, these imply that for the etched sample, the layer rich in Si element at the external surface (thickness of ~1.0 nm) is primarily removed by the etching method (Figure 1g). The terminal groups of these two samples in the hydroxyl region were identified by DRIFT as shown in Figure 1b. The characteristic IR signals at 3745 and 3678 cm^{-1} are assigned to isolated $\equiv$Si−O−H and $\equiv$P−O−H groups,[45] respectively. Two signals are visible at 3796 and 3770 cm^{-1}, assigned to −O−H groups lined to isolated tetrahedral Al.[45] In Figure 1b, the ratio of peak area between $\equiv$Si−O−H and $\equiv$Al−O−H for the pristine sample (~2.05) is higher than that for etched samples (~0.75). The ratio of $n(SiOH)/n(AlOH)$ is defined as the peak area ratio of IR spectroscopy at ~3740 cm^{-1} to that at ~3770 cm^{-1}. In Figure 1f, the quantitative ^{1}H MAS NMR spectra show a consistent amount of Brønsted acid sites (BAS) of pristine and etched samples (~0.90 mmol·g^{-1}). The amount of isolated silanol in the etched sample (~0.12 mmol·g^{-1}) is lower than that in the pristine sample (~ 0.18 mmol·g^{-1}), which results from the changes in the silicon-rich layer at surface termination by acid etching. As shown in Figure 1e, significant changes in silicon coordination detected by ^{29}Si MAS NMR were observed. Based on the previous studies,[45,46] it is shown that the signal position of Si atoms at −85, −89, −95, −99, −105, and −112 ppm correspond to $Si(OAl)_n(OH)_{4-n}$, Si(4Al), Si(3Al), Si(2Al), Si(1Al), and Si(0Al) components, respectively. In Table S2, by use of the deconvolution method, it can be found that after etching, the proportion of $Si(OAl)_n(OH)_{4-n}$ as terminal silanols[45,46] in the etched sample (5.1%) is lower than that in the pristine sample (9.3%). Meanwhile, the proportion of penta-coordinated aluminum in the etched sample (10.1%) is slightly higher than that in the pristine sample (7.3%), which indicates more exposure of aluminum species at termination by etching. From the elaborate characterizations of pristine and etched H-SAPO-34, it can be concluded that the removed layer at termination of the pristine sample with a thickness of ~1.0 nm is rich in the silicon-containing substance and $\equiv$Si−O−H terminal groups. Correspondingly, as shown in Figure 1g, the speculative models including the external surface and intracrystalline period structure for pristine and etched samples are proposed for multiscale simulations. In the following, the effect of such a layer on the molecule−external interface interaction is investigated.

In Figures 1i and S13, the DFT calculation shows that the adsorption energy of the molecule (e.g., water and propylene, respectively) adsorbed at the $\equiv$Si−O−H (e.g., $\Delta G_{ads}(H_2O) = 2.9$ kJ mol^{-1}) site is way lower than that at the $\equiv$Al−O−H site ($\Delta G_{ads}(H_2O) = 10.1$ kJ mol^{-1}). However, the adsorption energy of propane at $\equiv$Si−O−H or $\equiv$Al−O−H site shows no distinct difference. In Figure 1h, etched H-SAPO-34 (contact angle of water of ~58.9°) shows more hydrophobicity than that of the pristine H-SAPO-34 (contact angle of water of ~42.4°), which verifies the results of DFT calculations in Figure 1i. These results validate that the external crystal surface rich in $\equiv$Si−O−H groups (pristine H-SAPO-34) presents a stronger adsorption interaction on polar molecules and double bond of alkenes. In addition, we compared the adsorption heat ΔH_{ads} by simulations and experiments as shown in Figure S11 and Table S5, which validates the simulation results of ΔG_{ads} in Figures 1i and S13. Such discrepancy in the adsorption interaction caused by different amounts of isolated silanol may differ in the behavior of the surface barrier of guests.
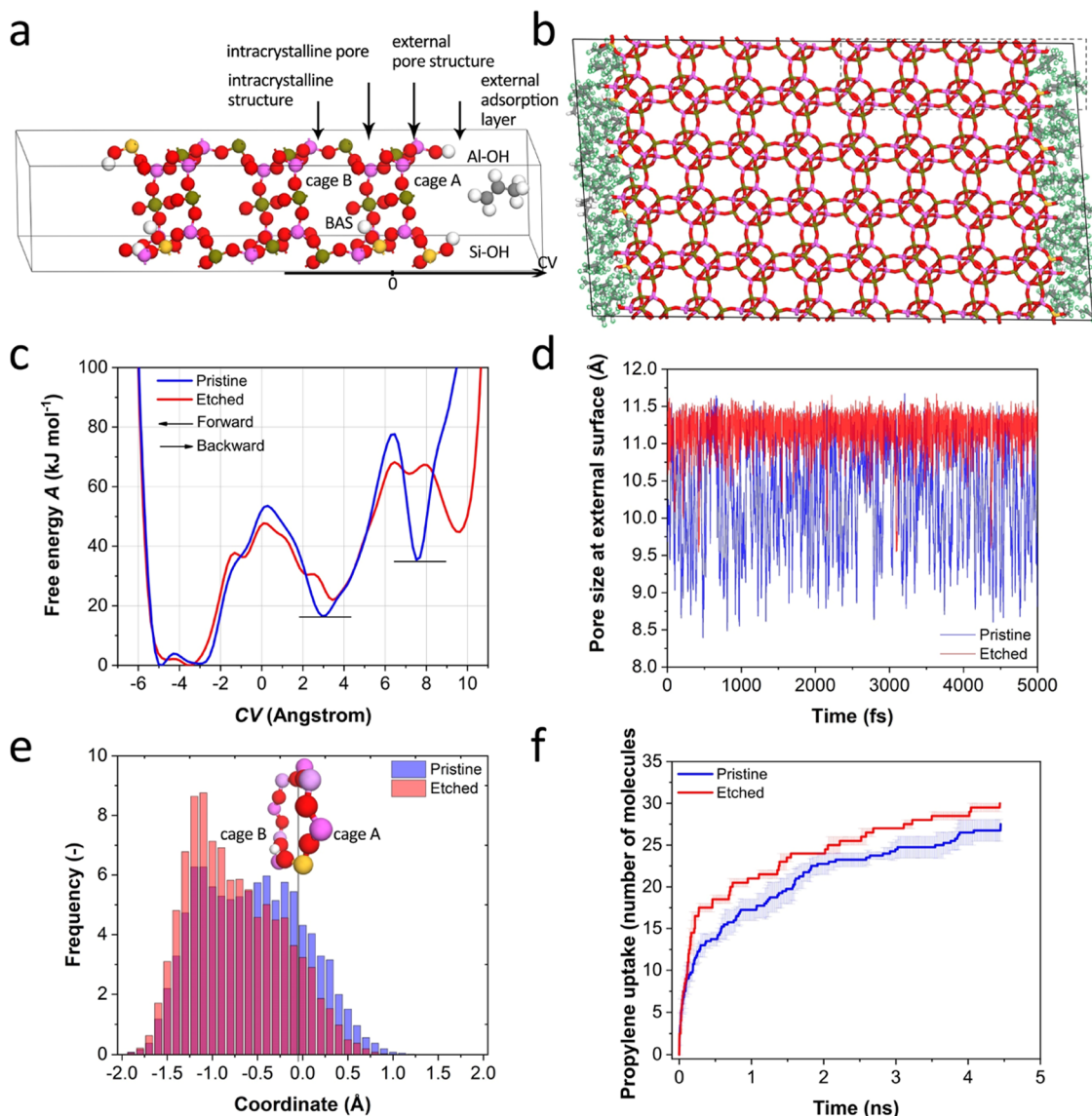
Figure 2. (a) Model of H-SAPO-34 zeolite with terminated groups of $\equiv$Si$-$O$-$H employed for AIMD. (b) Model of H-SAPO-34 zeolite with terminated groups of $\equiv$Si$-$O$-$H employed for the FFMD calculations. Local structure marked by a dashed line as input for AIMD. (c) Free energy profiles of propylene along the gas-phase, external crystal surface and intracrystalline structure of H-SAPO-34 zeolite at 298 K from AIMD simulations. (d) Time evolution of the pore size at the external surface of pristine and etched H-SAPO-34 models during regular AIMD simulations at 298 K. (e) Sampling distribution of the BAS proton as a function of the coordinate during a regular AIMD simulation at 298 K of propylene diffusion within pristine and etched H-SAPO-34. (f) Number of propylene molecules adsorbed in the internal H-SAPO-34 zeolite with different terminated hydroxyl groups as a function of time at 298 K from FFMD simulations. (Pristine model: $\equiv$Si$-$O$-$H as a main terminated group and etched model: $\equiv$Al$-$O$-$H as a terminated group).

4.2. Effect of Isolated Silanol on the Local Structure and Surface Diffusion Barriers. The diffusion of guest molecules from the gas phase to the internal structure of zeolites involves three steps (Figure 2a): (1) adhering to the external adsorption layer of zeolite from the gas phase; (2) leaving the external adsorption layer and jumping into the external pore structure (free energy barrier ΔF_{surf}); and (3) crossing intracrystalline pore and then diffusion within the intracrystalline structure of zeolite (free energy barrier ΔF_{inter}), which are shown in Supporting Video 1 and 2. The structures of $AlPO_4$ (CHA topology) with $\equiv$Si$-$O$-$H terminal groups (Figure 2b) and such structures without $\equiv$Si$-$O$-$H terminal groups (Figure S16b) were constructed for the FFMD simulations.[47,48] In Figure 2a, for instance, local structures close to the external surface marked by dashed lines in Figure

2b are extracted for the implementation of AIMD simulations. As shown in Figure 2c, the forward free energy barrier of the surface barrier $\Delta F_{surf}^{forward}$ (from the external adsorption layer to the external pore structure) for the pristine model is distinctly higher than that for the etched model. Based on the DFT calculations shown in Figure S13a,b, the adsorption of propylene on the $\equiv$Si$-$O$-$H site (ΔG_{ads} = 19.7 kJ/mol) is more preferential than that on the $\equiv$Al$-$O$-$H site (ΔG_{ads} = 23.4 kJ/mol). In Figure 2c, the x-coordinate from right to left represents the diffusion of propylene from the gas phase to the external surface and then to the intracrystalline phase. It can be found that for a CV of 7~10 Å, the calculated free energy of propylene on the pristine sample is lower than that on the etched one, which partially contributes a high diffusion barrier at the external surface of the pristine sample. Therefore, the$\equiv$
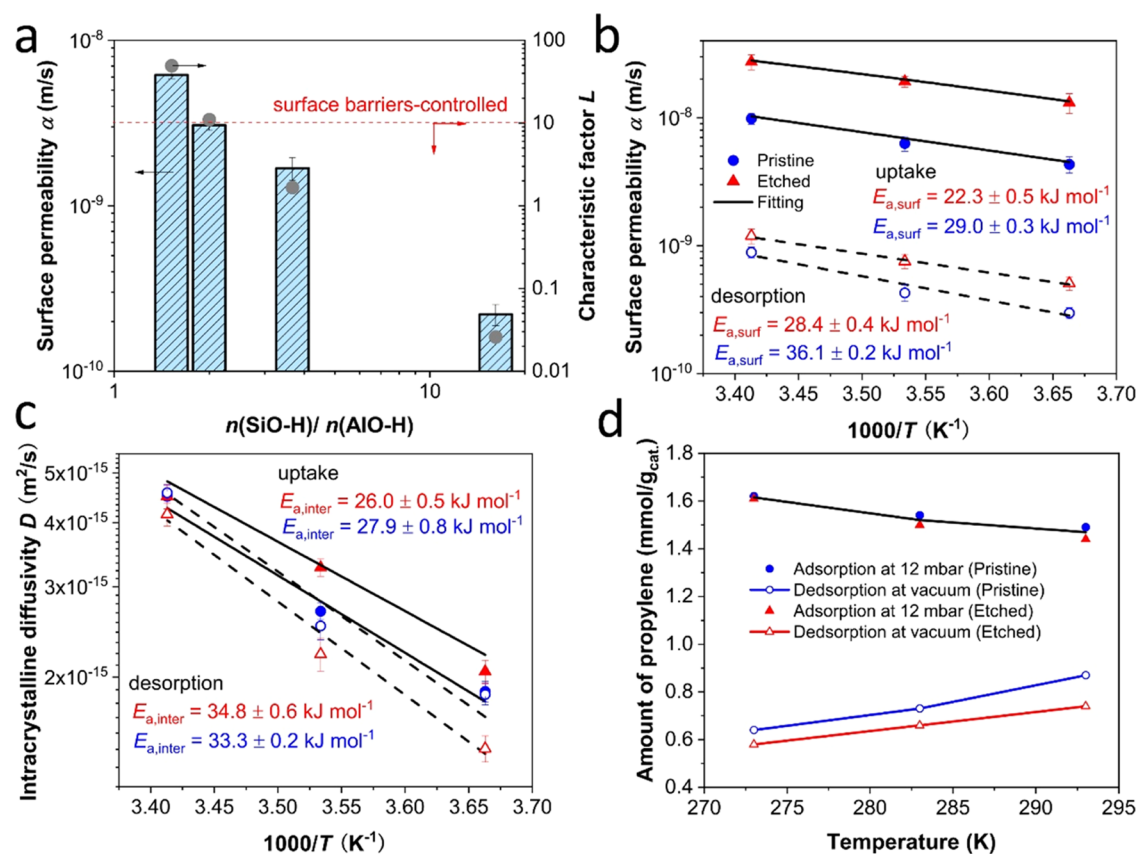
Figure 3. (a) Relationship between the ratio of $n(\equiv Si-O-H)/\ n(\equiv Al-O-H)$ and surface permeability of propane in H-SAPO-34 zeolites. Arrhenius plots of (b) surface permeability and (c) intracrystalline diffusivity and corresponding diffusion activation energy for pristine and etched H-SAPO-34. Solid points and solid lines are data obtained from the uptake process, and hollow points and dotted lines are data obtained from desorption process. (d) Adsorption amount of propylene at 12 mbar and residual amount of propylene after desorption at vacuum for pristine and etched H-SAPO-34 samples under 273, 283, and 293 K.

Si−O−H group can preferentially stabilize the adsorption state of propylene (pristine model) and leads to the retention of propylene at the external adsorption layer. Interestingly, we found the backward free energy barrier of the surface barrier $\Delta F_{surf}^{backward}$ (from the same structure close to the intracrystalline pore to the external pore structure) for model with the $\equiv$Si−O−H terminal group also exceeds for the model without the $\equiv$Si−O−H terminal group. In Figure 2d, typically (~5000 fs), the dynamic changes of the external 8MR pore of pristine and etched model during regular AIMD simulations are presented. The statistically average 8MR pore sizes at the external surface for pristine and etched models are 10.2 and 11.1 Å, respectively. This interprets that the vibration or flexibility of 8MR at the external surface can be affected by the type of linked terminal groups. The narrow of 8MR at the external surface does not directly result from the proton at $\equiv$Si−O−H. The detailed mechanism of such phenomena needs to be further explored by advanced experiments. The pore size analysis in Figure S2b is indirectly validated simulation results. This indicates that the type of terminal groups at the external zeolite surface has a crucial role in determining external 8MR pores, which can directly lead to a distinct behavior of surface barriers. In brief, using AIMD simulations, it can be clearly concluded that the external surface of zeolites decorated with $\equiv$Si−O−H groups can stabilize the adsorption of guest molecules and narrow the 8MR pore at termination. Therefore, the external surface with $\equiv$Si−O−H groups directly results in a higher free energy barrier of surface barriers during molecular uptake and desorption. For the diffusion from the intracrystalline pore to the intracrystalline structure within pristine and etched models, free energy barriers ΔF_{inter} show only small differences as shown in Figure 2c. The asymmetric profile in Figure 2c for intracrystalline diffusion of propylene can be elucidated by the preference location of the BAS proton for a specific cage due to the inherent puckering of 8MR pores,[49] which is shown in Figure 2e. In addition, the slight distinction in ΔF_{inter} between pristine and etched models states that altering the terminal groups of the external surface has a minor effect on intracrystalline diffusion of guest molecules. FFMD was implemented to simulate the diffusion of ensemble molecules from the gas-phase, external surface with different terminal groups to the internal structure of H-SAPO-34. In Figure 2f, the uptake of propylene by crossing the external adsorption layer with $\equiv$Si−O−H groups (pristine model) is obviously more sluggish than that by crossing the layer without $\equiv$Si−O−H groups (etched model). Particularly, the initial uptake amount of propylene in the etched model is ~1.6 times higher than that in the pristine model. Implementation of AIMD and FFMD synergistically elaborates the presence of terminal $\equiv$Si−O−H groups at the external surface can retard the permeation of alkenes through the external adsorption layer by enhancing the adsorption interaction and narrowing the 8MR pore.

To validate the results of MD simulations, the experimental measurements of surface permeability α, intracrystalline diffusivity D, and corresponding diffusion activation energies
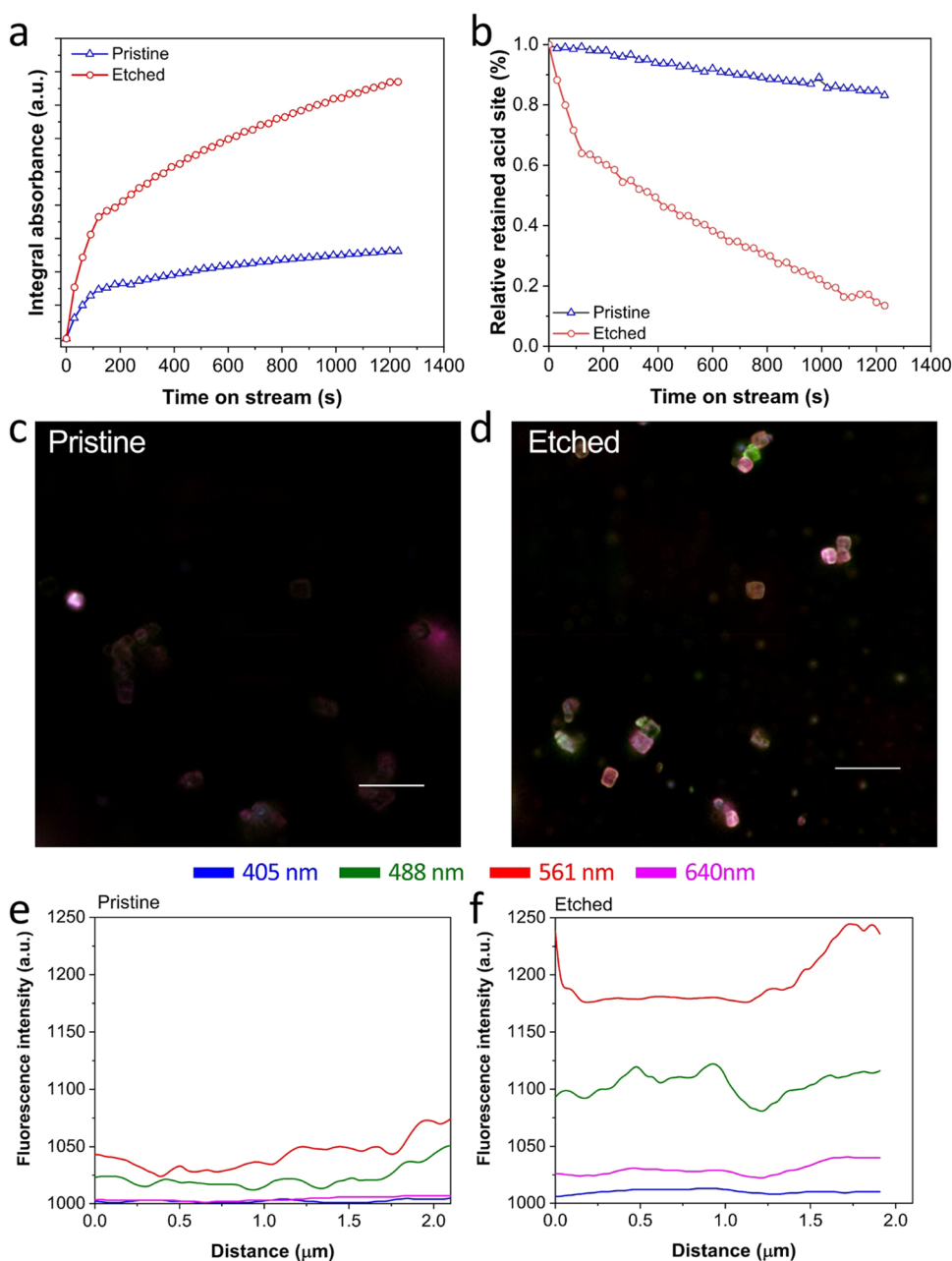
Figure 4. (a) Evolution of the stretching vibration of the C−H bond (alkyl groups on oligomers) within pristine and etched H-SAPO-34 zeolites during the propylene polymerization reaction obtained by integration of the IR signal at 2800−3000 cm^{-1} in Figure S9. (b) Relatively quantitative evolution of residual Brønsted acidity inside pristine and etched H-SAPO-34 zeolites of the IR signal at 3500−3700 cm^{-1}. Spatial distribution of coke species within individual (c) pristine and (d) etched H-SAPO-34 zeolite crystals observed by super-resolution SIM. Scale bar: 5 μm. The fluorescence intensities within the typical crystal are also displayed in (e) and (f). A laser excitation of 405 nm (detection at 435−485 nm, false color: blue), 488 nm (detection at 500−545 nm, false color: green), 561 nm (detection at 570−640 nm, false color: red), and 640 nm (detection at 663−738 nm, false color: pink). The images were taken in the middle plane of the zeolite crystal. The inlet of propylene is 5 mL/min, and the loading of catalysts is 10 mg at 373 K.

E_a over pristine and etched H-SAPO-34 samples were carried out. In Figure 3a, the characteristic factor L is defined as the ratio of characteristic time of intracrystalline diffusion to that of surface barriers in mass transfer. The smaller the L, the higher the surface barriers in overall mass transfer. In Figure 3a, when L becomes below 10, the surface barriers would play the leading role in mass transfer resistance, which refers to "surface barrier-controlled".[25] In Figure 3a, as the relative proportion between ≡Si−O−H and ≡Al−O−H at the external surface increases, propane's dominated mass transfer mechanism in H-

SAPO-34 becomes surface barrier-controlled. As evidenced by DFT calculations (Figure S13c,d), the adsorption of propane at ≡Si−O−H and ≡Al−O−H shows no apparent difference. The discrepant behavior in surface barriers of propane in pristine and etched samples can be interpreted as the narrowed pore size at the external surface caused by ≡Si−O−H groups (Figure 2d). In Figure 3b, the surface permeability of propylene over the etched sample is visibly higher than that over the pristine sample. According to the previous studies,[17,50] the diffusion activation energy (E_a) can be calculated by
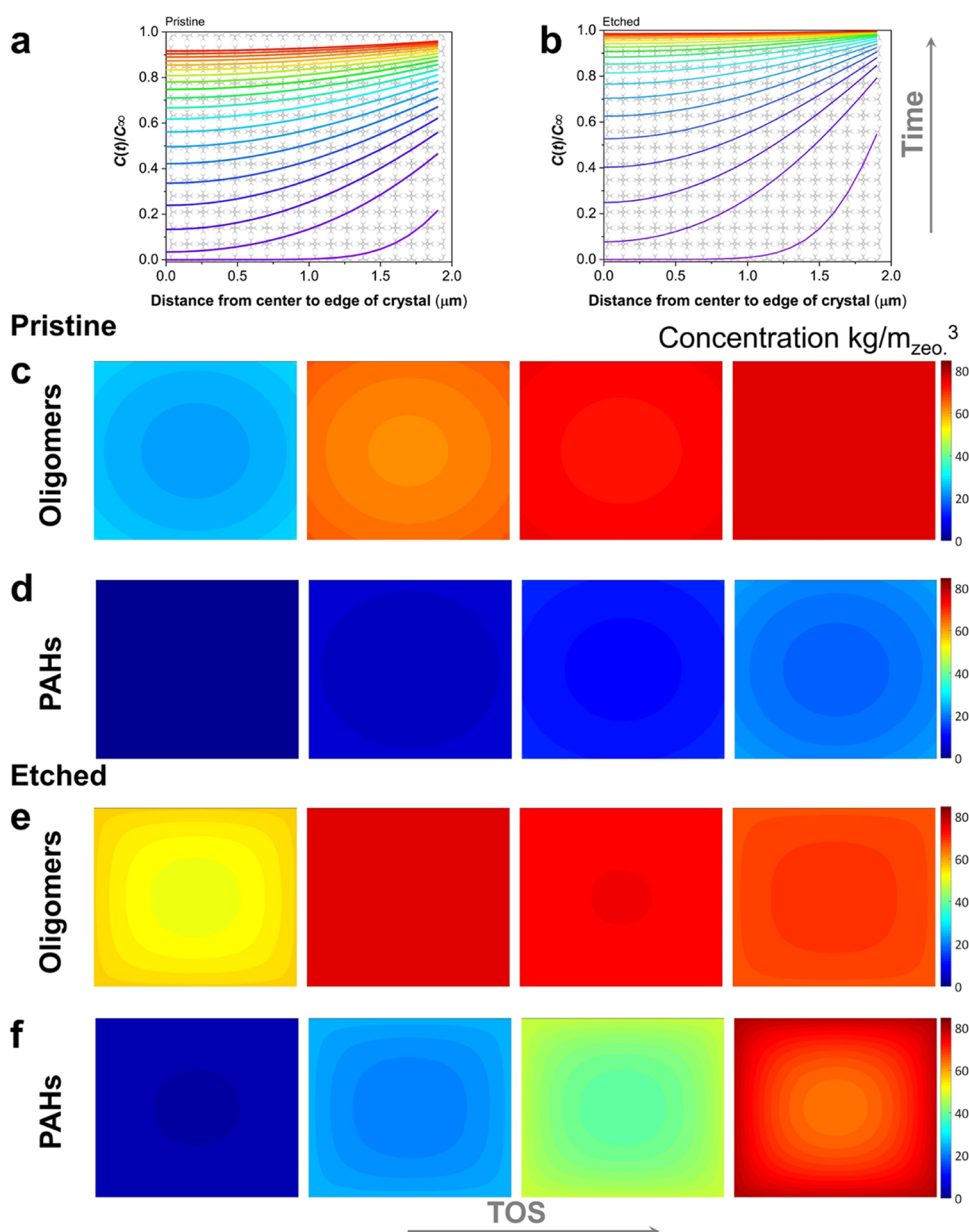
Figure 5. Spatiotemporal evolution of propylene in (a) pristine and (b) etched H-SAPO-34 samples at 373 K. Spatiotemporal evolution of oligomers and PAHs in (c and d) pristine and (e and f) etched H-SAPO-34 zeolite crystals during the propylene polymerization reaction at 313 K from reaction mass transfer simulations.

assuming that the relation between surface permeability/intracrystalline diffusivity and temperature follows the Arrhenius law $D = D_0 \exp(-E_a/RT)$. Thus, we can fit the data in Figure 3b,c with the Arrhenius equation and obtain E_a. As expected, the activation energy of the surface barrier $E_{a,surf}$ for the etched sample is lower than that for the pristine sample, which is in line with AIMD simulations. Based on the DFT simulations, the $\equiv$Si−O−H terminal groups favor the adsorption of propylene. Additionally, AIMD simulations show that the average 8MR size at the external surface linked to $\equiv$Si−O−H groups is smaller than that linked to $\equiv$Al−O−H groups. In Figure 1, the ratio of $n(\equiv$Si−O−H$)/n(\equiv$Al−O−H$)$ of the etched sample is smaller than that of the pristine sample. Therefore, the wakened adsorption interaction together with the relatively larger pore size of 8MR at the external surface reduces the $E_{a,surf}$ of propylene for the etched sample, while the intracrystalline diffusivities and activation

energy $E_{a,inter}$ of propylene over these two samples are almost equal (Figure 3c). This can illustrate that the etching method employed in this work only alters the surface barriers of guest molecules. In this work, we found that etching can remove a layer of ∼1.0 nm at termination of pristine H-SAPO-34 zeolites, and this layer is rich in the silicon-containing substance and $\equiv$Si−O−H terminal groups. The $\equiv$Si−O−H terminal groups can change the adsorption of guest molecules and alter the average size of the corresponding linked 8MR at the external surface. In Figure 3d, the identical adsorption amount of propylene at 12 mbar over pristine and etched samples (∼1.6 mmol g$_{cat.}^{-1}$) suggests that the influence of the surface barrier on adsorption equilibrium can be neglected. Interestingly, in Figures 3d and S10, it can be observed that the amount of propylene in the micropore is higher on desorption than on adsorption. As shown in Figures 3c and S8, the intracrystalline diffusivity of propylene based on the desorption

rate is lower than that based on the uptake rate. This implies that the stabilization on propylene imposed by Brønsted acid sites or nanoconfinement of the CHA cavity makes propylene difficult to desorption. Such a difference between uptake and desorption supported by experimental data indicates the asymmetry in adsorption and desorption paths from the external crystal surface to the intracrystalline region or other way around. Actually, Valiullin et al.[51] also obtained a similar conclusion in their study on mesoporous materials. In Figure 3c, it can be observed that the intracrystalline desorption rate is slower than the intracrystalline uptake rate, which is caused by the biased location of BAS at specific CHA cavity shown in Figure 2e. For the state of adsorption equilibrium, the preferential adsorption site of propylene is the BAS located at cage B (~84% probability), where the BAS can well interact with olefins by forming a π-complex.[49] Such asymmetric distribution of olefin adsorption at BAS directly leads to the backward diffusion barrier (intracrystalline desorption) is about 8 kJ mol^{-1} (Figure 3c) higher than the forward diffusion barrier (intracrystalline uptake), which is well elucidated by AIMD simulations. In Figure 3b, the surface permeability of propylene for desorption is an order of magnitude lower than that for uptake. From AIMD simulations, there is ~12% probability that BAS is located at cage A, which is close to the surface pore structure due to the mobility of BAS. In addition, the stabilization of olefin adsorption (π-complex host−guest interaction) by BAS is superior to that by the $\equiv$Si−O−H site. Thus, the diffusion barrier for desorption from the external pore structure at BAS is higher than that for uptake from the external layer with $\equiv$Si−O−H groups. Herein, the asymmetric diffusion path of adsorption and desorption for intracrystalline diffusion and surface barrier are well interpreted by experiments combined with AIMD simulations.

4.3. Role of Surface Barriers in Utilization of the Intracrystalline Active Site.
The role of terminal groups ($\equiv$Si−O−H and $\equiv$Al−O−H) at the external zeolite layer in surface permeation of guests has been well elucidated using a complementary set of surface modification, multiple spectroscopic techniques, MD simulations, and diffusion rate measurements. To build a comprehensive relationship of structure−mass transfer−performance, propylene polymerization catalyzed by H-SAPO-34 zeolite was used as a probe reaction to investigate the effect of the surface barrier on catalyst deactivation by coke deposition.[52] The detailed evolutions of hydroxyl groups and carbonaceous species within H-SAPO-34 were recorded by in situ Fourier transform infrared (FTIR) spectroscopy as shown in Figure S12. The overlapping bands at 2960 and 2930 cm^{-1} are, respectively, assigned to the CH$_3$− and −CH$_2$− asymmetric stretching vibrations of the oligomers. The theoretical intensity (I) of the CH$_3$− band is $8.0n + 258$ and that of the −CH$_2$− band is $77n − 18$, where n is the number of methylene groups in the chain.[53] Using a relative intensity ratio of $I_{2960}/I_{2930} = 1.1$, n is found to be ca. 4, which implies that the oligomer is formed from two propylene molecules. In Figure 4a, it can be observed that during propylene polymerization, the integrated intensity of IR spectra at 2800−3000 cm^{-1} in the etched H-SAPO-34 zeolite is significantly higher than that in the pristine sample. Similarly, the intensity of bands at 1460 and 1637 cm^{-1} in the etched sample, which are assigned to the C=C bond of polycyclic aromatic hydrocarbon (PAH), is also higher than that in pristine. The etched H-SAPO-34 sample can be 2.5 times higher in the formation rate of intermediate and 4 times

higher in the capacity of oligomers within zeolites than its counterpart with slow surface permeability of guests (Figure 4a). As shown in Figure 4b, compared to the BAS accessibility of the pristine sample, the intracrystalline region within the etched sample can be more accessible to propylene. Thus, for the deactivated catalyst by coke deposition, the etched H-SAPO-34 sample can be 14 times higher in BAS utilization than for the pristine sample.

To gain insights into the effect of surface barriers on coke deactivation within zeolites, reaction kinetics combined with mass transfer was analyzed. The reaction network was simplified as propylene oligomerization with BAS (reaction energy barrier $\Delta G^{\ddagger}$ is 104.7 kJ mol^{-1}, $k = 2.2 \times 10^{-2}$ s^{-1}) and cyclization of polyenes ($\Delta G^{\ddagger}$ is 80.2 kJ mol^{-1}, $k = 5.8 \times 10^1$ s^{-1}), and the corresponding reaction kinetics were obtained by DFT calculations[54] (Figure S14). The surface permeability, intracrystalline diffusivity, and diffusion-activated energy of propylene in pristine and etched samples were measured by experiments (Figure 3). In Figure 5a,b, enhancing the surface permeability of guests can increase the propylene concentration gradient close to the crystal edge and boost the mass flux (intracrystalline concentration) of propylene from the gas phase to the intracrystalline region. In fact, this has been directly observed in experiments of methanol diffusion over individual H-SAPO-34 zeolite crystals by use of interference microscopy.[55] Thus, at the initial moment, the accessibility of BAS in the etched H-SAPO-34 is more sufficient to propylene (Figure S15b). In Figure 5c,e, the amounts of oligomers formed within the etched sample are significantly higher than those within the pristine sample. This can be validated by TGA experiments; the coke amount of the deactivated etched sample (5.7%) is higher than that of the deactivated pristine sample (3.2%). In addition, the spatial distribution of oligomers in the etched is relatively uniform, while the oligomers are concentrated close to the rim of the pristine crystal. Due to the high concentration gradient of propylene at the rim of the etched sample (Figure 5b), subsequently, the PAHs are preferentially formed at the rim of the crystal. According to the results of MD simulations, the diffusion of light hydrocarbons will be impeded by PAHs trapped within the CHA cavity.[35] Thus, for the stage of catalyst deactivation, in the etched sample, the accessibility of oligomers located at the crystal center is prevented in contact with propylene. For the pristine sample, inherent low-surface permeability and PAHs formed at the rim of the crystal jointly hinder the diffusion of propylene from the gas phase to the intracrystalline region. Therefore, the concentration of PAHs deposited within the pristine crystal is significantly lower than that within the etched sample. In Figure 4c,d, spatial distributions of oligomers and PAHs within the deactivated pristine and etched H-SAPO-34 were visualized by super-resolution structured illumination microscopy (SIM) to validate simulation results (Figure 4c,d). For the deactivated pristine H-SAPO-34, the fluorescence signals detected at 500−545 nm (a laser excitation of 488 nm) and 570−640 nm (a laser excitation of 561 nm), which are assigned as oligomers and PAHs, respectively, are slightly strong at the crystal rim than at the interior crystal (Figure 4e). Under a similar measurement, the fluorescence signal of oligomers in the etched sample is concentrated on the crystal center. In contrast, the fluorescence signal of PAHs is mainly detected at the rim of the crystal (Figure 4f). These results validate the simulation presented in Figure 5c−f and visualize

the effect of surface barriers on the catalytic efficiency of zeolites.

5. CONCLUSIONS

In summary, we demonstrate that isolated silanol at zeolite termination can not only enhance the adsorptive interaction between the polar molecules or double bond of alkenes and external surface but also narrow the local 8MR pore entrances. Thus, isolated silanol exposed at termination can significantly retard the permeation of guest molecules through the external layer. In addition, the presence of isolated silanol at the external surface is the crucial origin for an asymmetric molecular diffusion path between uptake and desorption. Sluggish surface permeability of guest molecules directly leads to the low accessibility of intracrystalline BAS and catalytic activity of zeolites. Based on the structure−mass transfer−performance relationship, this work indicates that moderate etching to reduce the relative proportion of isolated silanol at zeolite termination can be considered an efficient method to increase both the surface permeability of guests and utilization efficiency of active sites. Importantly, future work in tailoring the external surface properties of zeolite should focus on modifying or grafting functional terminal groups[31] at zeolite termination, which may reform the catalytic performance of zeolites.

◼ ASSOCIATED CONTENT

Ⓢ Supporting Information

The Supporting Information is available free of charge at https://pubs.acs.org/doi/10.1021/acscatal.3c01932.

    SAPO-34_SiOH_diffusion_MD (MP4)

    SAPO-34_AlOH_diffusion_MD (MP4)

    Experimental and theoretical calculation details, catalyst characterization, and additional results (PDF)

◼ AUTHOR INFORMATION

Corresponding Author

Mao Ye − National Engineering Research Center of Lower-Carbon Catalysis Technology, Dalian Institute of Chemical Physics, Chinese Academy of Sciences, Dalian 116023, People's Republic of China; ⓞ orcid.org/0000-0002-7078-2402; Email: maoye@dicp.ac.cn

Authors

Mingbin Gao − National Engineering Research Center of Lower-Carbon Catalysis Technology, Dalian Institute of Chemical Physics, Chinese Academy of Sciences, Dalian 116023, People's Republic of China; ⓞ orcid.org/0000-0002-7143-2658

Hua Li − National Engineering Research Center of Lower-Carbon Catalysis Technology, Dalian Institute of Chemical Physics, Chinese Academy of Sciences, Dalian 116023, People's Republic of China

Yu Tian − National Engineering Research Center of Lower-Carbon Catalysis Technology, Dalian Institute of Chemical Physics, Chinese Academy of Sciences, Dalian 116023, People's Republic of China; University of Chinese Academy of Sciences, Beijing 10049, People's Republic of China

Junyi Yu − National Engineering Research Center of Lower-Carbon Catalysis Technology, Dalian Institute of Chemical Physics, Chinese Academy of Sciences, Dalian 116023,

People's Republic of China; University of Chinese Academy of Sciences, Beijing 10049, People's Republic of China

Zhongmin Liu − National Engineering Research Center of Lower-Carbon Catalysis Technology, Dalian Institute of Chemical Physics, Chinese Academy of Sciences, Dalian 116023, People's Republic of China; University of Chinese Academy of Sciences, Beijing 10049, People's Republic of China

Complete contact information is available at:
https://pubs.acs.org/10.1021/acscatal.3c01932

Author Contributions

The article was written through contributions of all authors. All authors have given approval to the final version of the article.

Notes

The authors declare no competing financial interest.

◼ ACKNOWLEDGMENTS

◼ REFERENCES

(1) Liu, L.; Corma, A. Confining isolated atoms and clusters in crystalline porous materials for catalysis. *Nat. Rev. Mater.* **2021**, *6*, 244−263.

(2) Dusselier, M.; Davis, M. E. Small-pore zeolites: synthesis and catalysis. *Chem. Rev.* **2018**, *118*, 5265−5329.

(3) Yarulina, I.; Chowdhury, A. D.; Meirer, F.; Weckhuysen, B. M.; Gascon, J. Recent trends and fundamental insights in the methanol-to-hydrocarbons process. *Nat. Catal.* **2018**, *1*, 398−411.

(4) Zimmerman, P. M.; Tranca, D. C.; Gomes, J.; Lambrecht, D. S.; Head-Gordon, M.; Bell, A. T. Ab Initio Simulations Reveal that Reaction Dynamics Strongly Affect Product Selectivity for the Cracking of Alkanes over H-MFI. *J. Am. Chem. Soc.* **2012**, *134*, 19468−19476.

(5) Qi, L.; Zhang, Y.; Conrad, M. A.; Russell, C. K.; Miller, J.; Bell, A. T. Ethanol Conversion to Butadiene over Isolated Zinc and Yttrium Sites Grafted onto Dealuminated Beta Zeolite. *J. Am. Chem. Soc.* **2020**, *142*, 14674−14687.

(6) Chi, X.; Li, M.; Di, J.; Bai, P.; Song, L.; Wang, X.; Li, F.; Liang, S.; Xu, J.; Yu, J. A highly stable and flexible zeolite electrolyte solid-state Li−air battery. *Nature* **2021**, *592*, 551−557.

(7) Li, Y.; Yu, J. Emerging applications of zeolites in catalysis, separation and host−guest assembly. *Nat. Rev. Mater.* **2021**, *6*, 1156−1174.

(8) Fu, D.; Park, Y.; Davis, M. E. Confinement effects facilitate low-concentration carbon dioxide capture with zeolites. *Proc. Natl. Acad. Sci. U.S.A.* **2022**, *119*, No. e2211544119.

(9) Medeiros-Costa, I. C.; Dib, E.; Nesterenko, N.; Dath, J.-P.; Gilson, J.-P.; Mintova, S. Silanol defect engineering and healing in zeolites: opportunities to fine-tune their properties and performances. *Chem. Soc. Rev.* **2021**, *50*, 11156−11179.

(10) Chizallet, C. Toward the Atomic Scale Simulation of Intricate Acidic Aluminosilicate Catalysts. *ACS Catal.* **2020**, *10*, 5579−5601.

(11) Dib, E.; Clatworthy, E. B.; Cruchade, H.; Medeiros-Costa, I. C.; Nesterenko, N.; Gilson, J.-P.; Mintova, S. Exploration, explanation

and exploitation of hydroxyls in zeolites. *Natl. Sci. Rev.* **2022**, *9*, No. nwac081.

(12) Vogt, C.; Weckhuysen, B. M. The concept of active site in heterogeneous catalysis. *Nat. Rev. Chem.* **2022**, *6*, 89−111.

(13) Karwacki, L.; Kox, M. H. F.; de Winter, D. A. M.; Drury, M. R.; Meeldijk, J. D.; Stavitski, E.; Schmidt, W.; Mertens, M.; Cubillas, P.; John, N.; Chan, A.; Kahn, N.; Bare, S. R.; Anderson, M.; Kornatowski, J.; Weckhuysen, B. M. Morphology-dependent zeolite intergrowth structures leading to distinct internal and outer-surface molecular diffusion barriers. *Nat. Mater.* **2009**, *8*, 959−965.

(14) Lupulescu, A. I.; Rimer, J. D. In Situ Imaging of Silicalite-1 Surface Growth Reveals the Mechanism of Crystallization. *Science* **2014**, *344*, 729−732.

(15) Le, T. T.; Qin, W.; Agarwal, A.; Nikolopoulos, N.; Fu, D.; Patton, M. D.; Weiland, C.; Bare, S. R.; Palmer, J. C.; Weckhuysen, B. M.; Rimer, J. D. Elemental zoning enhances mass transport in zeolite catalysts for methanol to hydrocarbons. *Nat. Catal.* **2023**, *6*, 254−265.

(16) Zhu, Y.; Ciston, J.; Zheng, B.; Miao, X.; Czarnik, C.; Pan, Y.; Sougrat, R.; Lai, Z.; Hsiung, C.-E.; Yao, K.; Pinnau, I.; Pan, M.; Han, Y. Unravelling surface and interfacial structures of a metal−organic framework by transmission electron microscopy. *Nat. Mater.* **2017**, *16*, 532−538.

(17) Hibbe, F.; Chmelik, C.; Heinke, L.; Pramanik, S.; Li, J.; Ruthven, D. M.; Tzoulaki, D.; Kärger, J. The Nature of Surface Barriers on Nanoporous Solids Explored by Microimaging of Transient Guest Distributions. *J. Am. Chem. Soc.* **2011**, *133*, 2804−2807.

(18) Kärger, J.; Binder, T.; Chmelik, C.; Hibbe, F.; Krautscheid, H.; Krishna, R.; Weitkamp, J. Microimaging of transient guest profiles to monitor mass transfer in nanoporous materials. *Nat. Mater.* **2014**, *13*, 333−343.

(19) Guo, Z.; Li, X.; Hu, S.; Ye, G.; Zhou, X.; Coppens, M.-O. Understanding the Role of Internal Diffusion Barriers in Pt/Beta Zeolite Catalyzed Isomerization of n-Heptane. *Angew. Chem., Int. Ed.* **2020**, *59*, 1548−1551.

(20) Reitmeier, S. J.; Gobin, O. C.; Jentys, A.; Lercher, J. A. Enhancement of Sorption Processes in the Zeolite H-ZSM5 by Postsynthetic Surface Modification. *Angew. Chem., Int. Ed.* **2009**, *48*, 533−538.

(21) Choudhary, M. K.; Jain, R.; Rimer, J. D. In situ imaging of two-dimensional surface growth reveals the prevalence and role of defects in zeolite crystallization. *Proc. Natl. Acad. Sci. U.S.A.* **2020**, *117*, 28632−28639.

(22) Dai, H.; Shen, Y.; Yang, T.; Lee, C.; Fu, D.; Agarwal, A.; Le, T. T.; Tsapatsis, M.; Palmer, J. C.; Weckhuysen, B. M.; Dauenhauer, P. J.; Zou, X.; Rimer, J. D. Finned zeolite catalysts. *Nat. Mater.* **2020**, *19*, 1074−1080.

(23) Zhao, D.; Tian, X.; Doronkin, D. E.; Han, S.; Kondratenko, V. A.; Grunwaldt, J.-D.; Perechodjuk, A.; Vuong, T. H.; Rabeah, J.; Eckelt, R.; Rodemerck, U.; Linke, D.; Jiang, G.; Jiao, H.; Kondratenko, E. V. In situ formation of ZnOx species for efficient propane dehydrogenation. *Nature* **2021**, *599*, 234−238.

(24) Li, X.; Wang, J.; Liu, X.; Liu, L.; Cha, D.; Zheng, X.; Yousef, A. A.; Song, K.; Zhu, Y.; Zhang, D.; Han, Y. Direct Imaging of Tunable Crystal Surface Structures of MOF MIL-101 Using High-Resolution Electron Microscopy. *J. Am. Chem. Soc.* **2019**, *141*, 12021−12028.

(25) Gao, M.; Li, H.; Yang, M.; Gao, S.; Wu, P.; Tian, P.; Xu, S.; Ye, M.; Liu, Z. Direct quantification of surface barriers for mass transfer in nanoporous crystalline materials. *Commun. Chem.* **2019**, *2*, 43−52.

(26) Teixeira, A. R.; Chang, C.-C.; Coogan, T.; Kendall, R.; Fan, W.; Dauenhauer, P. J. Dominance of Surface Barriers in Molecular Transport through Silicalite-1. *J. Phys. Chem. C* **2013**, *117*, 25545−25555.

(27) Zhang, B.; Li, G.; Liu, S.; Qin, Y.; Song, L.; Wang, L.; Zhang, X.; Liu, G. Boosting Propane Dehydrogenation over PtZn Encapsulated in an Epitaxial High-Crystallized Zeolite with a Low Surface Barrier. *ACS Catal.* **2022**, *12*, 1310−1314.

(28) Peng, S.; Gao, M.; Li, H.; Yang, M.; Ye, M.; Liu, Z. Control of surface barriers in mass transfer to modulate methanol-to-olefins

reaction over SAPO-34 zeolites. *Angew. Chem., Int. Ed.* **2020**, *59*, 21945−21948.

(29) Hu, S.; Liu, J.; Ye, G.; Zhou, X.; Coppens, M.-O.; Yuan, W. Effect of External Surface Diffusion Barriers on Platinum/Beta-Catalyzed Isomerization of n-Pentane. *Angew. Chem., Int. Ed.* **2021**, *60*, 14394−14398.

(30) Cao, K.; Fan, D.; Gao, M.; Fan, B.; Chen, N.; Wang, L.; Tian, P.; Liu, Z. Recognizing the Important Role of Surface Barriers in MOR Zeolite Catalyzed DME Carbonylation Reaction. *ACS Catal.* **2022**, *12*, 1−7.

(31) Jin, Z.; Wang, L.; Zuidema, E.; Mondal, K.; Zhang, M.; Zhang, J.; Wang, C.; Meng, X.; Yang, H.; Mesters, C.; Xiao, F.-S. Hydrophobic zeolite modification for in situ peroxide formation in methane oxidation to methanol. *Science* **2020**, *367*, 193−197.

(32) Liu, X.; Shi, J.; Yang, G.; Zhou, J.; Wang, C.; Teng, J.; Wang, Y.; Xie, Z. A diffusion anisotropy descriptor links morphology effects of H-ZSM-5 zeolites to their catalytic cracking performance. *Commun. Chem.* **2021**, *4*, No. 107.

(33) Yuan, J.; Liu, Z.; Wu, Y.; Han, J.; Tang, X.; Li, C.; Chen, W.; Yi, X.; Zhou, J.; Krishna, R.; Sastre, G.; Zheng, A. Thermal resistance effect on anomalous diffusion of molecules under confinement. *Proc. Natl. Acad. Sci. U.S.A.* **2021**, *118*, No. e2102097118.

(34) Kärger, J.; Ruthven, D. M.; Theodorou, D. N. *Diffusion in Nanoporous Materials*; Wiley-VCH Verlag & Co., KGaA, 2012.

(35) Gao, M.; Li, H.; Liu, W.; Xu, Z.; Peng, S.; Yang, M.; Ye, M.; Liu, Z. Imaging spatiotemporal evolution of molecules and active sites in zeolite catalyst during methanol-to-olefins reaction. *Nat. Commun.* **2020**, *11*, No. 3641.

(36) Wang, J.-Y.; Mangano, E.; Brandani, S.; Ruthven, D. M. A review of common practices in gravimetric and volumetric adsorption kinetic experiments. *Adsorption* **2021**, *27*, 295−318.

(37) Lu, T.; Chen, F. Multiwfn: A multifunctional wavefunction analyzer. *J. Comput. Chem.* **2012**, *33*, 580−592.

(38) Frisch, M. J.; Trucks, G. W.; Schlegel, H. B.; Scuseria, G. E.; Robb, M. A.; Cheeseman, J. R.; Scalmani, G.; B, V.; Petersson, G. A.; Nakatsuji, H.; Li, X.; Caricato, M.; Marenich, A.; Bloino, J.; Janesko, B. G.; Gomperts, R.; Mennucci, B.; Hratchian, H. P.; Ortiz, J. V.; Izmaylov, A. F.; Sonnenberg, J. L.; Williams-Young, D.; Ding, F.; L, F.; Egidi, F.; G, J.; Peng, B.; P, A.; Henderson, T.; Ranasinghe, D.; Zakrzewski, V. G.; Gao, J.; Rega, N.; Zheng, G.; Liang, W.; Hada, M.; Ehara, M.; Toyota, K.; Fukuda, R.; Hasegawa, J.; Ishida, M.; Nakajima, T.; Honda, Y.; Kitao, O.; Nakai, H.; Vreven, T.; Throssell, K.; Montgomery, J. A., Jr.; P, J. E.; Ogliaro, F.; Bearpark, M.; Heyd, J. J.; Brothers, E.; Kudin, K. N.; Staroverov, V. N.; Keith, T.; Kobayashi, R.; Normand, J.; Raghavachari, K.; Rendell, A.; Burant, J. C.; Iyengar, S. S.; Tomasi, J.; Cossi, M.; Millam, J. M.; Klene, M.; Adamo, C.; Cammi, R.; Ochterski, J. W.; Martin, R. L.; Morokuma, K.; Farkas, O.; Foresman, J. B.; Fox, D. J. *Gaussian 09*, revision B.01 edn; Gaussian, Inc., 2016.

(39) VandeVondele, J.; Krack, M.; Mohamed, F.; Parrinello, M.; Chassaing, T.; Hutter, J. QUICKSTEP: Fast and accurate density functional calculations using a mixed Gaussian and plane waves approach. *Comput. Phys. Commun.* **2005**, *167*, 103−128.

(40) Jürg, H.; Marcella, I.; Florian, S.; Joost, V. Atomistic simulations of condensed matter systems. *Wiley Interdiscip. Rev.: Comput. Mol. Sci.* **2014**, *4*, 15−25.

(41) Combariza, A. F.; Sastre, G. Influence of Zeolite Surface in the Sorption of Methane from Molecular Dynamics. *J. Phys. Chem. C* **2011**, *115*, 13751−13758.

(42) Hansen, N.; Krishna, R.; van Baten, J. M.; Bell, A. T.; Keil, F. J. Analysis of Diffusion Limitation in the Alkylation of Benzene over H-ZSM-5 by Combining Quantum Chemical Calculations, Molecular Simulations, and a Continuum Approach. *J. Phys. Chem. C* **2009**, *113*, 235−246.

(43) Hansen, N.; Kerber, T.; Sauer, J.; Bell, A. T.; Keil, F. J. Quantum Chemical Modeling of Benzene Ethylation over H-ZSM-5 Approaching Chemical Accuracy: A Hybrid MP2:DFT Study. *J. Am. Chem. Soc.* **2010**, *132*, 11525−11538.

(44) Tian, P.; Wei, Y.; Ye, M.; Liu, Z. Methanol to Olefins (MTO): From Fundamentals to Commercialization. *ACS Catal.* **2015**, *5*, 1922−1938.

(45) Li, Z.; Martinez-Triguero, J.; Concepcion, P.; Yu, J.; Corma, A. Methanol to olefins: activity and stability of nanosized SAPO-34 molecular sieves and control of selectivity by silicon distribution. *Phys. Chem. Chem. Phys.* **2013**, *15*, 14670−14680.

(46) Buchholz, A.; Wang, W.; Arnold, A.; Xu, M.; Hunger, M. Successive steps of hydration and dehydration of silicoaluminophosphates H-SAPO-34 and H-SAPO-37 investigated by in situ CF MAS NMR spectroscopy. *Microporous Mesoporous Mater.* **2003**, *57*, 157−168.

(47) Sastre, G.; Kärger, J.; Ruthven, D. M. Molecular Dynamics Study of Diffusion and Surface Permeation of Benzene in Silicalite. *J. Phys. Chem. C* **2018**, *122*, 7217−7225.

(48) Knio, O.; Fang, H.; Boulfelfel, S. E.; Nair, S.; Sholl, D. S. Molecular Dynamics Investigation of Surface Resistances in Zeolite Nanosheets. *J. Phys. Chem. C* **2020**, *124*, 15241−15252.

(49) Cnudde, P.; Demuynck, R.; Vandenbrande, S.; Waroquier, M.; Sastre, G.; Speybroeck, V. V. Light Olefin Diffusion during the MTO Process on H-SAPO-34: A Complex Interplay of Molecular Factors. *J. Am. Chem. Soc.* **2020**, *142*, 6007−6017.

(50) Gao, S.; Liu, Z.; Xu, S.; Zheng, A.; Wu, P.; Li, B.; Yuan, X.; Wei, Y.; Liu, Z. Cavity-controlled diffusion in 8-membered ring molecular sieve catalysts for shape selective strategy. *J. Catal.* **2019**, *377*, 51−62.

(51) Valiullin, R.; Naumov, S.; Galvosas, P.; Kärger, J.; Woo, H.-J.; Porcheron, F.; Monson, P. A. Exploration of molecular dynamics during transient sorption of fluids in mesoporous materials. *Nature* **2006**, *443*, 965−968.

(52) Duan, J.; Chen, W.; Wang, C.; Wang, L.; Liu, Z.; Yi, X.; Fang, W.; Wang, H.; Wei, H.; Xu, S.; Yang, Y.; Yang, Q.; Bao, Z.; Zhang, Z.; Ren, Q.; Zhou, H.; Qin, X.; Zheng, A.; Xiao, F.-S. Coking-Resistant Polyethylene Upcycling Modulated by Zeolite Micropore Diffusion. *J. Am. Chem. Soc.* **2022**, *144*, 14269−14277.

(53) Ghosh, A. K.; Kydd, R. A. A Fourier-transform infrared spectral study of propene reactions on acidic zeolites. *J. Catal.* **1986**, *100*, 185−195.

(54) Van Speybroeck, V.; Van der Mynsbrugge, J.; Vandichel, M.; Hemelsoet, K.; Lesthaeghe, D.; Ghysels, A.; Marin, G. B.; Waroquier, M. First Principle Kinetic Studies of Zeolite-Catalyzed Methylation Reactions. *J. Am. Chem. Soc.* **2011**, *133*, 888−899.

(55) Remi, J. C. S.; Lauerer, A.; Chmelik, C.; Vandendael, I.; Terryn, H.; Baron, G. V.; Denayer, J. F. M.; Karger, J. The role of crystal diversity in understanding mass transfer in nanoporous materials. *Nat. Mater.* **2016**, *15*, 401−406.